

The shocked molecular layer in RCW 120

M. S. Kirsanova,¹* Ya. N. Pavlyuchenkov,¹ A. O. H. Olofsson,² D. A. Semenov,^{3,4} A. F. Punanova⁵

¹*Institute of Astronomy, Russian Academy of Sciences, 119017, 48 Pyatnitskaya Str., Moscow, Russia*

²*Department of Space, Earth and Environment, Chalmers University of Technology, Onsala Space Observatory, SE-43992 Onsala, Sweden*

³*Max-Planck-Institut für Astronomie, Königstuhl 17, 69117 Heidelberg, Germany*

⁴*Department of Chemistry, Ludwig Maximilian University, Butenandtstraße 5–13, 81377 Munich, Germany*

⁵*Ural Federal University, 620002, 19 Mira street, Yekaterinburg, Russia*

Accepted XXX. Received YYY; in original form ZZZ.

ABSTRACT

Expansion of wind-blown bubbles or H II regions lead to formation of shocks in the interstellar medium, which compress surrounding gas into dense layers. We made spatially and velocity-resolved observations of the RCW 120 PDR and nearby molecular gas with CO(6–5) and ¹³CO(6–5) lines and distinguished a bright CO-emitting layer, which we related with the dense shocked molecular gas moving away from the ionizing star due to expansion of H II region. Simulating gas density and temperature, as well as brightness of several CO and C+ emission lines from the PDR, we found reasonable agreement with the observed values. Analysing gas kinematics, we revealed the large-scale shocked PDR and also several dense environments of embedded protostars and outflows. We observe the shocked layer as the most regular structure in the CO(6–5) map and in the velocity space, when the gas around YSOs is dispersed by the outflows.

Key words: shock waves – ISM: kinematics and dynamics – photodissociation region (PDR) – submillimetre: ISM

1 INTRODUCTION

Massive stars shape the Galaxy via radiative and mechanical feedback and appear as lighthouses of star formation. The feedback is primarily visible through optical emission of ionized (H II) regions in the plane of the Galaxy (e. g. recent H-alpha surveys by [Gustad et al. 2001](#); [Drew et al. 2005](#)). Theory predicts that shock waves, related to expansion of the H II regions, compress the neutral gas and dust and collect it into moving dense molecular layers, (e.g. [Spitzer 1978](#)). One of the most studied dense shocked layers on the border of an H II region is the Orion Bar photo-dissociation region (PDR, the region between ionization front and attenuated cold molecular gas), which has already been observed with high angular resolution in optical, infrared and millimetre wavelengths (e. g. [McLeod et al. 2016](#); [Goicoechea et al. 2016](#); [Berné et al. 2022](#)). A steady-state structure of the Orion Bar PDR where dissociation fronts of different molecules are separated from each other by several values of A_V was developed by [Tielens & Hollenbach \(1985\)](#); [Tielens et al. \(1993\)](#). Only after the appearance of the first ALMA data towards the PDR, dynamical effects have been revealed by [Goicoechea et al. \(2016\)](#) and confirmed numerically by [Kirsanova & Wiebe \(2019\)](#). Since the Orion Bar PDR is a unique object due to its proximity, many other PDRs are all less studied. Moreover, retirement of the SOFIA telescope, which brought a bulk of important observational data towards PDRs, leads to difficulties in getting more data about PDRs. Therefore, our knowledge about PDRs are highly limited by the strong selection effect and every new study of their properties is important.

The southern H II region RCW 120 is powered by an O6-8V/III

ionizing star ([Martins et al. 2010](#)) and has a radius of 250''. Simple ring-like geometry of RCW 120, which resembles a projection of a 3D spherical shell, makes it attractive to study. However, the position of the ionizing star does not corresponds to the center of the neutral envelope of the H II region, see [Fig. 1](#). Moreover, the maximum of the free-free continuum emission is shifted to the south up to 1.5' in the plane of the sky. Therefore, the simple geometry of RCW 120 might be illusory. RCW 120 is one of the nearest H II regions to the Sun, 1.34 kpc distant ([Russeil 2003](#))¹. Physical radius of the H II region is therefore about 1.6 pc but the mean projected distance between the ionizing star and the southern neutral border of the H II region is about 1 pc. The cold neutral material around RCW 120 consists of several condensations arranged to the shell-like structure, the condensations contain embedded young stellar objects (YSOs) ([Zavagno et al. 2007](#); [Deharveng et al. 2009](#)). The most massive is a Class 0 YSO with $M_{\text{star}} = 8 - 10M_{\odot}$ (source 2 in [Figueira et al. \(2017\)](#), S2 below). Recently, [Luisi et al. \(2021\)](#) found an expanding continuous shell around RCW 120 due to a stellar wind impact, observing the C II emission at 158 μm .

The neutral environment of RCW 120 has different geometry compared with the view at the C II line. The PDR appeared in flattened face-on molecular cloud partly embedded into a low-density envelope (see [Anderson et al. 2015](#); [Kirsanova et al. 2019](#); [Kabanovic et al. 2022](#)). Therefore, RCW 120 is not a simple 3D sphere or 2D ring, but different parts of the object can be modelled by a 1D or 2D numerical model or by their combination. Modelling of the region

¹ We prefer not using 1.7 kpc from [Kuhn et al. \(2019\)](#) because GAIA gives the best distances for unobscured stars but the extinction $A_V = 4.4$ towards RCW 120, see [Zavagno et al. \(2007\)](#).

* E-mail: kirsanova@inasan.ru

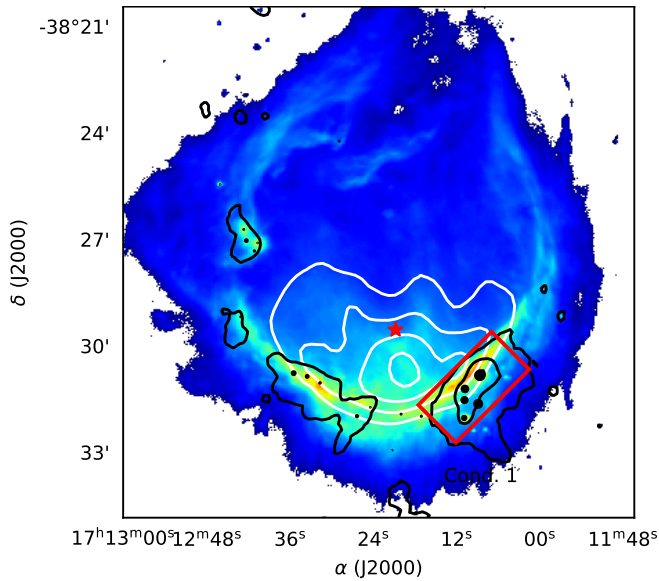


Figure 1. Image of RCW 120 at $70\mu\text{m}$. Color scale shows emission of neutral material around the ionized gas. The position of the ionizing star of RCW 120 is marked as a red star. The 843 MHz radio continuum emission corresponding to free-free emission of the ionized gas is shown with white contours linearly spaced from from 0.1 to 0.4 Jy/beam. The $870\mu\text{m}$ contours for 0.4, 2.0 and 10.0 Jy/beam are shown in black. Black circles show the locations of compact sources described by Figueira et al. (2017) (their Table 5). The sizes of the circles depend linearly on the source masses (M_{env} from Figueira et al. 2017) here and on the following figures. The area, observed in the CO(6–5) line, is shown by the red rectangle.

as a whole can probably be done in some approximation such as a smoothed-particle hydrodynamics approach (see Walch et al. 2015).

Since RCW 120 is expanding, one can expect to find the dense shocked layer in its PDR. While the mentioned above authors studied RCW 120 with spectral lines of CO and its isotopologues, none of these studies had sufficient spatial resolution to resolve the shocked layer. Kirsanova et al. (2019) calculated the physical structure of the RCW 120 PDR and found a width of the dense moving layer of 0.1 pc. Using single-dish ground-based telescopes, this layer can be resolved only with the APEX telescope and CO(6–5) lines at a frequency ≈ 660 GHz (Fig. 1 in Kirsanova 2018) or by ALMA. In this study, we present the resolved observations of the dense shocked layer in RCW 120.

2 OBSERVATIONAL DATA AND NUMERICAL SIMULATIONS

We performed new observations of the RCW 120 PDR and combined their results with simulations of the region in order to distinguish between large-scale phenomena, related to the kinematics of the H II region, and local star-formation processes, related to star-forming activity, on molecular emission maps.

2.1 CO(6–5) and ^{13}CO (6–5) observations

The observations were carried out using the Atacama Pathfinder Experiment telescope (APEX) in Chile on 15 and 17/18 of October 2019 and 10 July 2021, as projects O-0103.F-9301A-2020 and O-0107.F-9318A-2021 (PI: Kirsanova M. S.) within the Swedish oper-

ated share. The receiver used was the Band 9 part of the SEPIA bundle (Baryshev et al. 2015; Belitsky et al. 2018), also called SEPIA 660. In case of ^{12}CO (2019), it was tuned to 691 GHz (the line frequency is 691473.076 MHz) covering the sideband ranges 685–693 & 701–709 GHz, and for ^{13}CO (2021) it was tuned to 661067.276 MHz covering 655–663 & 671–679 GHz. The spectral resolution in the FFT spectrometer used was about 61 kHz (26 m s^{-1}) with 65536 channels per every 4 GHz. The data were calibrated to antenna temperature in real-time using the standard *apexOnlineCalibrator* package, but we later additionally applied factors of $\eta_{\text{mb}} = 0.40$ and 0.53 for CO(6–5) and ^{13}CO (6–5), respectively², to arrive at the main beam temperature scale. The spatial resolution of the data was $9''$, corresponded to 0.058 pc at the distance of RCW 120.

We observed a region with different physical conditions: from the irradiated side of molecular clump on the border of the ionization front (photo dissociation region, RCW 120 PDR below) to the outskirts of the clump, see Fig. 1. The region contains several massive YSOs. For ^{12}CO , the region was mapped using the OTF mapping mode to cover $175''$ by $90''$ rotated 45° in the equatorial system (the long side extending from southeast to northwest, see Fig. 1). The rows/columns in the map were alternately observed along the x- and y-directions with a data dump time of 1.0 seconds and a step of $3.1''$. The off-position was chosen at the direction $\alpha = 17^{\text{h}}12^{\text{m}}08.000^{\text{s}}$, $\delta = -38^{\circ}36'03.00''$ (J2000). The weather was rather poor with $0.9 < \text{PWV} < 1.6$ mm (corresponding to $T_{\text{sys}} \approx 1000 - 4000$ K) for the ^{12}CO map given this atmospheric window but relatively stable and calibrations were inserted more often to ensure consistent intensity calibration.

The ^{13}CO observations were carried out as a $90''$ OTF strip cutting through the peak integrated intensity position of the ^{12}CO map at a right angle to the long axis of the map. The data dump time and step size were the same as for the ^{12}CO observations. Total observational time was 1.7 h. The weather conditions were better for the ^{13}CO observations with $0.6 < \text{PWV} < 0.7$ mm and typical $T_{\text{sys}} = 730$ K.

The gridding of the data and the baseline correction were performed using the CLASS package from the GILDAS³ software. Further analysis was done with Astropy (Astropy Collaboration et al. 2013, 2018), and APLpy (Robitaille & Bressert 2012; Robitaille 2019) was used for representation. Final fits-cubes were proceeded to the common grid with the step size of $3.1''$ in x- and y-directions. Typical noise level (1σ) of the regridded data is 1.5–1.7 K.

2.2 Archival data

We used the multi-wavelength data from various archives. In the section, we briefly describe them and provide needed references. The *Herschel* HiGAL data at $70\mu\text{m}$ (Molinari et al. 2010) and the SUMSS 843 MHz radio continuum emission (Bock et al. 1999) were used to outline general geometry of the neutral environment RCW 120 and the ionized gas, respectively. The ATLASGAL $870\mu\text{m}$ emission was used to locate dense and cold molecular clumps (Schuller et al. 2009). The [C II] line emission at $158\mu\text{m}$ obtained as a part of the FEEDBACK Legacy Program (Schneider et al. 2020) were downloaded from the *SOFIA* archive and used to study the irradiated side of the RCW 120 PDR together with the *Spitzer* data at $8\mu\text{m}$ (Zavagno et al. 2007). We also used the ^{12}CO and ^{13}CO (3–2) data

² <https://www.apex-telescope.org/telescope/efficiency/index.php>

³ <http://www.iram.fr/IRAMFR/GILDAS>

(Kabanovic et al. 2022) to study dependence of our conclusions on spatial resolution.

2.3 Numerical simulations

We simulated the physical and chemical structure of RCW 120 using the MARION model according to the approach by Kirsanova et al. (2019). In the present study, all the model parameters were taken the same as those authors did. We took the model results at the moment 5.8×10^5 yrs from the beginning of the H II region expansion when the H II region has the radius about 1 pc. We note that this model time should not be considered as an age of RCW 120, because geometry of the region is not spherical and density distribution is not uniform. However, our 1D model can be used to study the shocked region on a scale of a particular molecular clump because we are not pretending to simulate the line profiles, related to geometry, but interested only in the line brightness, related to the energy of the region. Using the simulated physical and chemical structure, we applied RADEX software (Van der Tak et al. 2007) in order to model brightness of the various lines of CO, ^{13}CO and C II. Coefficients for collisions with H_2 were used for all considered emission lines because this molecule is the most abundant collision partner in our model. Using APEX beamwidth at 1.3, 0.9 and 0.4 mm ($27''$, $18''$ and $9''$) as well as *SOFIA* beamwidth at 158 micron ($15''$), we simulate the brightness of molecular lines from RCW 120 for those telescopes.

3 RESULTS

3.1 Observed CO(6–5) and ^{13}CO (6–5) line emission

Spatial distributions of the CO(6–5) peak and the integrated intensity are different as they are defined by large-scale and local phenomena, respectively. Namely, the peak intensity of the CO(6–5) emission in Fig. 2 has a layer-like spatial distribution coinciding with the [C II] emission in the RCW 120 PDR. The peak CO(6–5) intensity drops sharply on the irradiated side of the PDR but decreases smoothly on the attenuated side. The layer of the bright CO(6–5) emission appears parallel to the ionization front (compare Fig. 1 and 2) and does not become warped around the border of the dense and cold material, traced by ATLASGAL 870 μm contours (compare left and right panels in Fig. 2). Therefore, the bright CO-layer represents a shell of irradiated gas related to large-scale gas distribution created by RCW 120.

The shortest projected distance from the ionizing star (shown in Fig. 1) to the bright CO-layer is $146.5''$, corresponding to 0.9 pc. Physical width of the layer, in the direction perpendicular to the ionization front, is $\approx 0.10 - 0.15$ pc as we deduce from spatial distribution of the peak intensity in Fig. 2. Note that the width of the bright CO-layer remains almost the same over the entire region we observed in contrast with the [C II] and $8\mu\text{m}$ emission, shown in Fig. 2 and 3, whose widths become broader up to a factor of 1.5–2 in the south-eastern part of the observed region. Two of five massive YSOs, namely S2 and S10, are projected on the bright CO-layer, the other three massive YSOs are located outside the layer. Several point sources, found by Deharveng et al. (2009), (see Fig. 3), are located outside the CO-layer. Width of the whole molecular clump perpendicular to the ionization front is ≈ 0.4 pc.

On the other hand, the map of the integrated intensity reveals also rather local phenomena, related to regions of star-forming activity. Several peaks of the integrated CO(6–5) intensity appear towards YSOs but not towards the PDR's edge. Therefore, broadening of the

CO(6–5) lines towards the YSOs is responsible for the appearance of the integrated intensity peaks. The highest integrated intensity of CO(6–5) coincides with the peak of the ATLASGAL 870 μm emission and the most massive YSO S2. There are three minor peaks of the CO(6–5) emission towards YSOs S1, S10 and S39. There is one more massive YSO S9 in the map, but it does not demonstrate brightening of the CO(6–5) emission.

The regions affected by the large-scale (related with the expanding H II region) and local (related with the star-forming activity towards the YSOs) phenomena are clearly distinguishable in Fig. 4, where we show individual CO(6–5) and ^{13}CO (6–5) spectra. The CO(6–5) lines are single-peaked in positions 1–4 on the irradiated side of the PDR. Deeper to the molecular clump, the line profiles become double-peaked, less symmetric and demonstrate pronounced red and blue wings towards S2 (position 8). The irradiated side of the bright CO-layer demonstrates the narrowest width of the CO(6–5) and ^{13}CO (6–5) lines $\approx 4 \text{ km s}^{-1}$ over the entire map including the area without YSOs deeper to the molecular clump in positions 11–18.

Local star formation reveals itself through the wings of the CO(6–5) line clearly visible in positions 7–11. We find a narrow dip in the CO(6–5) profiles at -8 km s^{-1} , which we associate with a self-absorption effect. The ^{13}CO (6–5) line profiles are single-peaked everywhere except for the position 8, where velocities of the CO(6–5) and ^{13}CO (6–5)-dips on the double-peaked profiles are not the same, where the ^{13}CO (6–5) dip is shifted to the red by 1 km s^{-1} and the ^{13}CO (6–5) peak coincides with the CO(6–5)-dip. Therefore, these dips can be caused by different factors: self-absorption for CO(6–5) (also previously detected by Kirsanova et al. (2019); Figueira et al. (2020); Kabanovic et al. (2022) for the (2–1) and (3–2) transitions, but shifted to the blue side for the (1–0) transitions in Anderson et al. (2015)) and the gas infall for ^{13}CO (6–5), while the second statement requires further investigation using tracers of dense gas.

3.2 Simulated CO(6–5) and ^{13}CO (6–5) line emission

In order to study the origin of the bright CO-layer, we compare the observed CO(6–5) and ^{13}CO (6–5) intensities in the layer with results of numerical simulations. Fig. 5 shows the edge of the H II region and surrounding PDR, where gas temperature and density change up to several orders. The dense layer of the neutral material, which has been accumulated around the H II region by a shock wave, whose propagation preceded the expanding ionized gas. The shocked region contains the H/H₂ and C⁺/C/CO transition. The mass of the shocked region is mostly contained in the gas where hydrogen and carbon are in the forms of H₂ and CO, respectively. Even in the region, where carbon is in the form of C⁺, $n(\text{H}_2) > n(\text{H})$ up to factor of few. Carbon becomes doubly ionized in the H II region and distribution of C⁺ traces the irradiated border of the PDR. The outer attenuated border is located inside of the shocked layer, there the extinction reaches 10 and higher values. The width of the shocked layer is ≈ 0.1 pc.

It is seen from Fig. 5, that spatial distribution of brightness temperatures for the CO and ^{13}CO (2–1) and (3–2) line emission does not allow to resolve the thickness of the shocked layer. The peaks of the (2–1) transitions are shifted outside the PDR, the peak widths are two times broader than the layer, and the contrast between the peak and emission from undisturbed molecular gas is only 20–50%. The (3–2) transitions better trace the shocked layer, while the widths of the peaks are still broader and the contrast reaches only a factor of 3. Only the (6–5) line emission reaches its maximum exactly at the densest part of the shocked layer and has zero-to-zero width exactly the same as the width of the shocked layer. The peak of the simulated

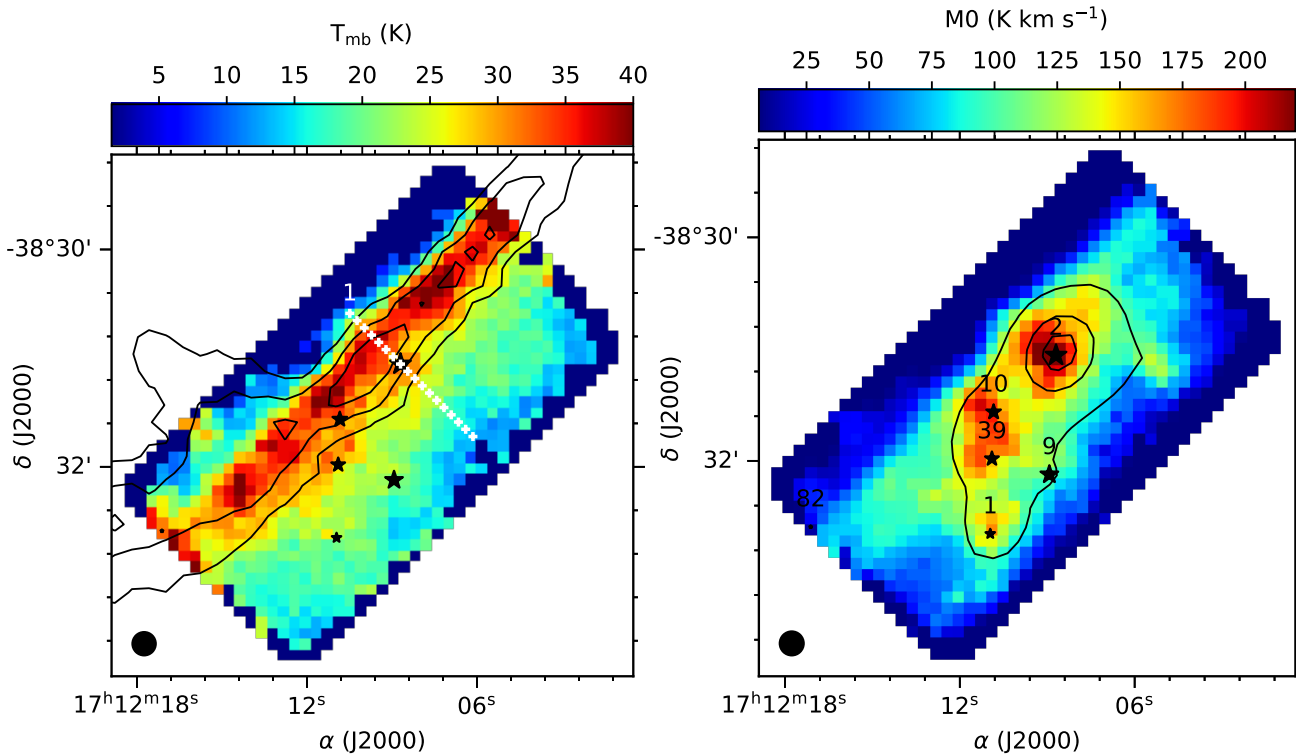


Figure 2. Left: map of the CO(6–5) peak intensity in the RCW 120 PDR shown by colour scale. Contours show brightness of the [C II] line emission at 20, 30 and 40 K. White crosses show positions of the $^{13}\text{CO}(6-5)$ spectra shown in Fig. 4, where position 1 corresponds to illuminated side of the PDR. Right: map of the CO(6–5) integrated intensity shown by colour scale. The 870 μm contours for 0.4, 2.0 and 10.0 Jy/beam are shown by contours. The APEX beam at 691 GHz is shown by black circle. The black stars show the locations of YSOs from [Figueira et al. \(2017\)](#) in both plots and in following figures.

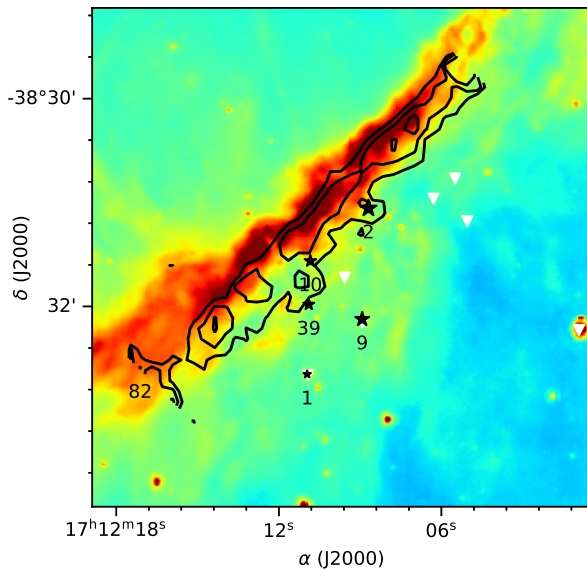


Figure 3. Image at $8\mu\text{m}$ and the map of the CO(6–5) peak intensity are shown by colour and contours, respectively. The contours are shown for 30, 35 and 40 K km s^{-1} . White triangles show YSOs from [Deharveng et al. \(2009\)](#).

C II emission is shifted to the ionizing star for less than the APEX beamsize at the 690 GHz. Simulated brightness of the CO(6–5) and $^{13}\text{CO}(6-5)$ lies in the interval and agrees with the low limit of the observed values, respectively, see Fig. 2 The simulated C II also lies in the observed interval of values, see contours in Fig. 2. Simulated

$^{13}\text{CO}(2-1)$ and $(3-2)$ lines intersect the ranges of the line brightness taken from [Kirsanova et al. \(2019\)](#).

Comparing the view of the bright CO-layer in Fig. 2 and results of the simulations in Fig. 5, we relate this layer with the shocked dense neutral material, which has been shovelled up on the border of the ionized region during hundreds of thousands of years. The shocked layer represents large-scale structure, related with evolution of the H II region. In RCW 120, we see the CO(6–5) emission also outside the shocked layer, probably due to local heating from embedded YSOs. Below we show how the shocked layer is displayed in the kinematic structure of the observed region.

4 PHYSICAL CONDITIONS IN MOLECULAR GAS

In this section we analyse radial distribution of excitation conditions for the CO(6–5) and $^{13}\text{CO}(6-5)$ lines using the LTE approach and also combine these data with available archival data for the non-LTE analysis in the most interesting directions of the observed region.

4.1 LTE

We show in Fig. 6 (top panel) radial profiles of the CO(6–5) peak brightness and integrated intensity, taken perpendicular to the PDR along the $^{13}\text{CO}(6-5)$ strip. Spatial difference between the maxima of the peak and integrated intensities $\approx 9''$, i.e. about the size of the telescope beam. Spatial behaviour of the $^{13}\text{CO}(6-5)$ peak intensities qualitatively resembles the CO(6–5) emission with the sharp/smooth decreasing on the inner/outer sides of the PDR. However, the $^{13}\text{CO}(6-5)$ integrated intensity shows almost symmetrical

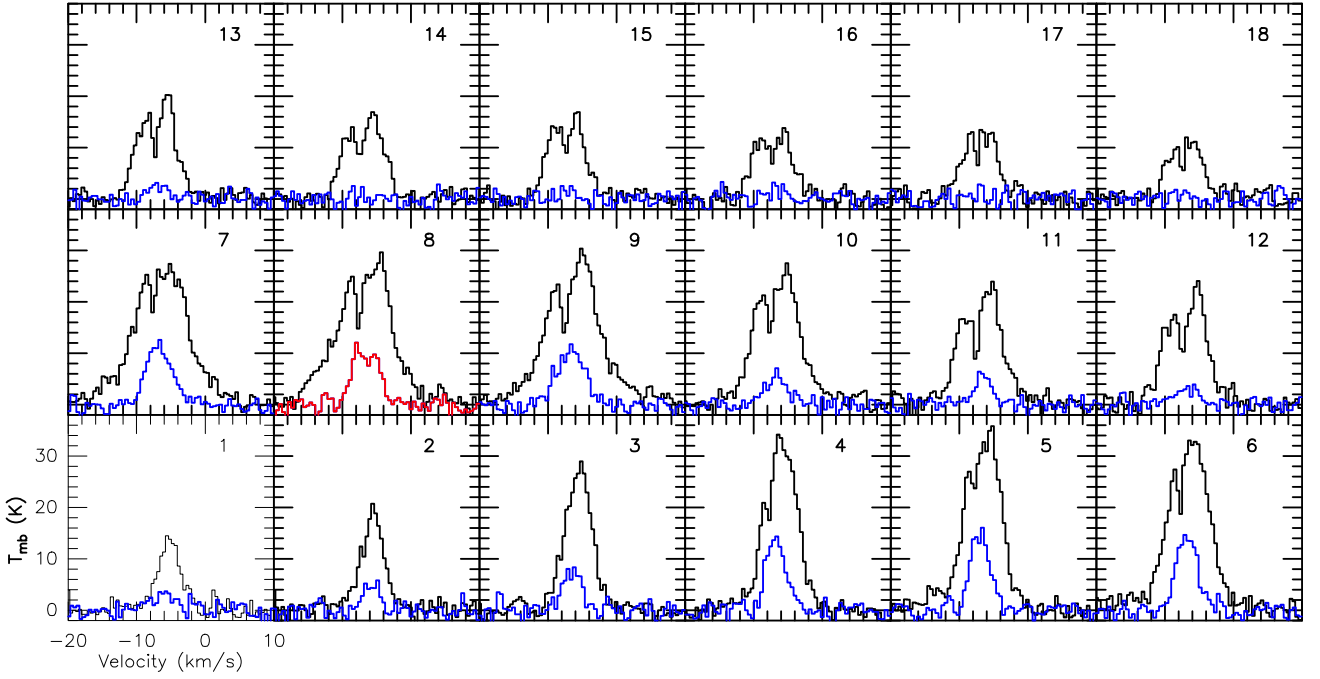


Figure 4. CO(6–5) (black) and ^{13}CO (6–5) (blue) spectra along the strip shown in Fig. 2. The spectra are shown with the step of $3''$ from the north-east (position 1 at the offset $\Delta\alpha, \Delta\delta = 21'', 21''$) to south-west (position 18 at the offset $\Delta\alpha, \Delta\delta = -30'', -30''$). Towards S2, the ^{13}CO (6–5) line is shown by red colour (position 8).

spatial distribution around the YSO 2 which can be related to its lower optical depth. Comparing the observed and simulated radial distributions in Fig. 5, we note that both the ^{13}CO (6–5) distributions are symmetric. However, there is no smooth decrease of the simulated CO(6–5) emission on the outer side of the shocked layer. We relate the enhancement of the observed CO(6–5) emission in positions 11–18 with local star-forming activity in the region, which is not included into our simulations.

With both the CO(6–5) and ^{13}CO (6–5) lines, along the same strip in molecular cloud, we estimate the optical depth of the CO(6–5) line and the CO column density using an LTE approach, explicitly described by Mangum & Shirley (2015), see Eq. (79) therein. This approach assumes the same constant excitation temperature (T_{ex}) for CO(6–5) and ^{13}CO (6–5) along the line of sight. For the (6–5) transition we used the energy of the upper level $E_u = 116.2$ K, rotation constant $B_0 = 55101.014 \times 10^6$ Hz, and dipole moment $\mu = 0.1$ Debye. Results of the LTE analysis: optical depth of the CO(6–5) line τ , excitation temperature T_{ex} and CO column density N_{CO} are shown in Fig. 6. In order to estimate uncertainties of T_{ex} , τ and N_{CO} , we varied integrated intensities of the CO(6–5) and ^{13}CO (6–5) lines as well as the ^{13}CO (6–5) brightness temperature within their 1σ intervals. Repeating the procedure 100 times, we find the average values of these parameters with their standard deviations.

The CO(6–5) lines are optically thick in all positions where we detect the ^{13}CO (6–5) emission with the CO(6–5) optical depth $\tau \approx 18 - 20$ in the direction of S2 and $10 \leq \tau \leq 20$ in the direction of the PDR. Dividing the τ value by the $^{12}\text{C}/^{13}\text{C}$ ratio = 61, suitable for the galactocentric distance of RCW 120 (Wilson 1999), we find optically thin ^{13}CO (6–5) line along the strip even in the direction of the YSO. The value of T_{ex} does not exceed 50 K and has almost flat radial profile along the strip within the interval of 40 – 50 K. As we work in the LTE approximation, we estimate thermal width of the CO(6–5) line using the T_{ex} value and find it ≤ 0.5 K. Optical

depth of the CO(6–5) line also contributes to the broadening by a factor of $\approx \log(\tau) \approx 2 - 3$, i. e. up to 1 km s^{-1} . Totally, thermal and depth-related broadening provide less than 25% of the observed line widths. Therefore, the widths of both CO(6–5) and ^{13}CO (6–5) lines from Fig. 4 are non-thermal, but the width of the self-absorption feature is thermal. Therefore, the self-absorption of these relatively high excitation lines ($E_u > 100$ K) can be caused by cool gas between RCW 120 and the observer.

CO column density distribution along the strip has two maximal values of $N_{\text{CO}} \approx 2 \times 10^{19} \text{ cm}^{-2}$ in the direction of the PDR and the YSO S2, respectively (spectra 1, 2 and 8 in Fig. 4). Using values of hydrogen column density from the ViaLactea survey (based on *Herschel* data, see Marsh et al. 2017), we determine relative abundance of CO in the bright CO-layer and other directions along the strip and find it $\sim 10^{-4}$. The CO/ H_2 ratio is close to the elemental abundance of carbon, H_2 and CO are well mixed with each other in the PDR and in the remaining part of the molecular clump also. Therefore, the CO and H_2 dissociation fronts should be situated closer to the ionizing star than position 1 in Fig. 2. While the ViaLactea maps may underestimate hydrogen column density, the uncertainty related to the *Herschel* fluxes does not significantly affect the densest regions, see, e. g. a comparison made by Ladeyschikov et al. (2021).

4.2 non-LTE

While straightforward LTE analysis allows estimating gas temperature (T_{gas}) in molecular gas, it doesn't give any information about the gas number density (n_{H_2}). Therefore, we combine the ^{13}CO (6–5) line emission data from the present study and the ^{13}CO (2–1) and ^{13}CO (3–2) data from Kirsanova et al. (2019), to estimate physical conditions in three different regions in RCW 120. Namely, towards the S2 YSO, to the PDR layer (position with the offset $\Delta\alpha, \Delta\delta = 20'', 20''$, between positions 1 and 2 in Fig. 2), and towards molecular cloud

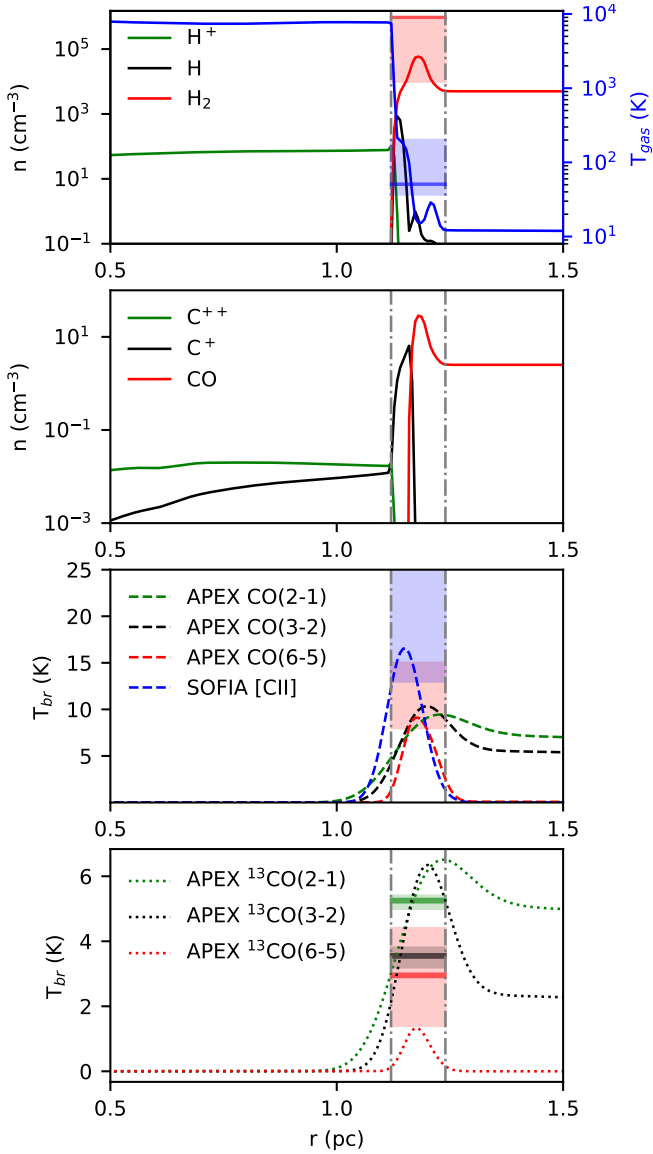


Figure 5. Simulated (lines) and observed (colour rectangles and horizontal straight lines) properties of the RCW 120 PDR. Simulated physical conditions and chemical composition in the dense neutral layer around the H II region obtained with the MARION model are shown on the two top panels. The ionizing star is located outside the left border of the panels in the beginning of the horizontal axis. The red rectangles and the red lines show the $\pm\sigma$ significance intervals and the best-fit solution of the non-LTE analysis with the observed and archival data (see Sec. 4). Simulated brightness of the C II, CO and ^{13}CO emission in different lines obtained with the RADEX software is shown in two bottom panels. Green and black horizontal colour bold lines and rectangles show the brightness and $\pm\sigma$ intervals for the archival $^{13}\text{CO}(2-1)$ and $^{13}\text{CO}(3-2)$ lines. The observed range of CO(6-5) and $^{13}\text{CO}(6-5)$ brightness are shown by the red rectangle. The $^{13}\text{CO}(6-5)$ brightness used for simulations with RADEX is shown by the red horizontal line.

($\Delta\alpha, \Delta\delta = -20'', -20''$, between positions 15 and 16), all positions are given relatively to the S2 YSO at $\alpha = 17^{\text{h}}12^{\text{m}}08.700^{\text{s}}$ and $\delta = -38^{\circ}30'46.40''$ (J2000). There are no YSOs in the PDR and MC directions, therefore we can obtain parameters of molecular gas without contamination of any activity related to star formation. We fixed the widths of all the CO lines to 4.4 km s^{-1} and background temperature to 2.7 K in order to calculate non-LTE models with

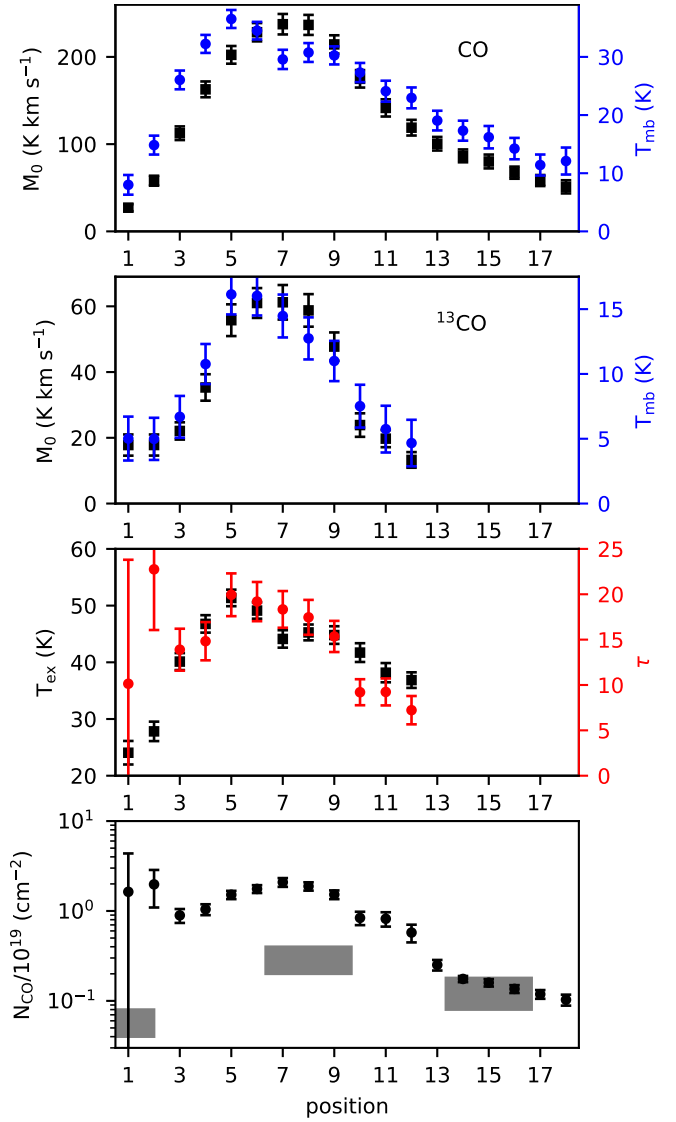


Figure 6. Integrated and peak intensities of the CO(6-5) and $^{13}\text{CO}(6-5)$ emission (two top panels) as well as the results of the LTE analysis along the cut. Position 8 corresponds to the direction to the Core 2 YSO. Grey rectangles at the bottom panel correspond to the ranges of N_{CO} from the non-LTE analysis.

RADEX software on a grid of different T_{gas} (from 10 to 200 K divided by 100 intervals), n_{H_2} ($10^3 - 10^7 \text{ cm}^{-3}$, 100 intervals), $N_{^{13}\text{CO}}$ ($10^{14} - 10^{18} \text{ cm}^{-2}$, 100 intervals). The best-fit results and $\pm\sigma$ significance intervals, found with the χ^2 -test (Wall & Jenkins 2003) are shown in Table 1. In order to estimate dependence of the χ^2 minimum on the noise level of the various ^{13}CO lines, we varied their integrated intensities within the 1σ levels: 0.3, 0.1 and 1.5 K for $^{13}\text{CO}(2-1)$, $^{13}\text{CO}(3-2)$ and $^{13}\text{CO}(6-5)$, respectively. Repeating the procedure by 100 times, we found the average minimum of the χ^2 value and corresponding average parameters with their standard deviations. For the YSO model, the average minimum T_{gas} and n_{H_2} with their standard deviations are shown in Fig. 7. Comparison of the error bars with the shape of the χ^2 dependency of the T_{gas} and n_{H_2} values shows that the quality of the observational data does not affect on the best-fit parameters, while the degeneracy of the best-fit parameters is significant due to the ^{13}CO line excitation conditions.

	T_{gas} (K)	n_{H_2} (10^4 cm^{-3})	$N_{^{13}\text{CO}}$ (10^{16} cm^{-2})
PDR	50_{37}^{200}	$950_{1.0}^{1000}$	$0.8_{0.6}^{1.1}$
Core 2 YSO	124_{40}^{200}	$1.3_{0.6}^{1000}$	$4.7_{4.3}^{6.1}$
MC	64_{22}^{200}	$1.5_{0.2}^{1000}$	$1.7_{1.3}^{2.8}$

Table 1. The best-fit results and $\pm\sigma$ significance intervals of non-LTE analysis for the Core 2 YSO, PDR and molecular cloud.

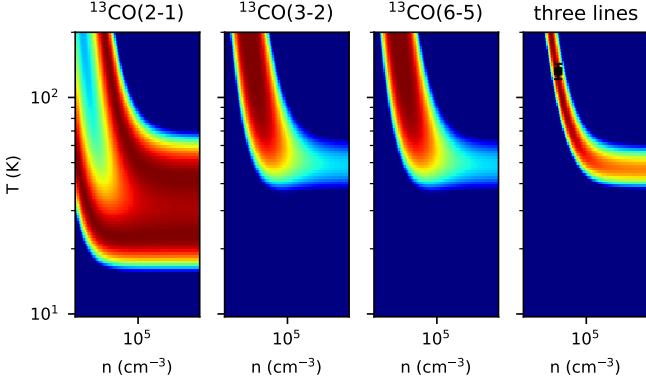


Figure 7. Grid of the ^{13}CO RADEX models for different gas temperatures and densities at the best-fit $N_{^{13}\text{CO}} = 4.7 \times 10^{16} \text{ cm}^{-2}$ for the S2 YSO position. Colour shows χ^2 where values are decreasing towards dark red.

However, we become convinced that the solution for the minimum is steady.

We find that the $N_{^{13}\text{CO}}$ value is determined with an accuracy of 30–60%, while the $\pm\sigma$ significance intervals are much broader for T_{gas} and n_{H_2} . Considering only those T_{gas} and n_{H_2} , which corresponds to the best-fit $N_{^{13}\text{CO}}$ values, we find almost the same intervals, those are shown in Fig. 7 for the YSO position (the χ^2 diagrams for the PDR and MC positions have similar shape). The value of T_{gas} from non-LTE analysis agrees within a factor of two with T_{ex} values from the LTE analysis in the PDR and MC positions, but the minimum χ^2 value was found at $T_{\text{gas}} = 124 \text{ K}$ towards the YSO. While the values of N_{CO} from LTE and non-LTE analysis are also in agreement within the uncertainty intervals (see the bottom panel in Fig. 6, where we show $N_{\text{CO}} = 61 \times N_{^{13}\text{CO}}$), the non-LTE value is lower by an order of magnitude towards S2. Therefore, the non-LTE effects of the line excitation are important towards the S2 YSO, but the LTE approximation is valid for the physical conditions in the MC position. The gas temperature $> 100 \text{ K}$, found in S2, agrees with the results by Kirsanova et al. (2021), who found hot gas towards the YSO.

The non-LTE intervals for the n_{H_2} and T_{gas} values at the PDR position agrees also with the simulated values in the shocked material, see Fig. 5. This agreement confirms that the bright CO-layer is the shocked gas indeed. The best-fit n_{H_2} value in the PDR position is by 2–2.5 orders of magnitude higher than that in the YSO and MC positions. We explain this fact by compactness of dense material in the direction of the YSO and relatively large beam size of our observations. The minimum non-thermal line width of the CO(6–5) line together with the high density of the PDR also indicate that the bright CO-layer might represent the gas where internal chaotic motions were suppressed by the shock.

5 KINEMATICS OF THE MOLECULAR GAS

Position-velocity (pv) diagrams in Fig. 8, made parallel and perpendicular to the ionization front, show complex structure of the observed region. Making the cuts perpendicular to the ionization front, we clearly see the bright CO-layer with narrow CO(6–5) lines, which we relate to the shocked layer. This gas is unperturbed by the embedded YSOs, see e. g. the diagram 1p at the offset $\approx 30''$. The lines become broader at the larger offsets ≈ 50 – $70''$ as we move away from the PDR to the molecular clump. All the observed line widths are non-thermal (see analysis of physical parameters in Sec. 4), therefore we suggest that the velocity dispersion can be decreased in the shocked layer due to compression (and higher turbulence decay) and star-forming activity leads to the broadening of the lines outside the layer. The pv diagram 2p demonstrate local gas kinematics related to star-forming activity in the S2 YSO, namely broad lines with wings at the offset ≈ 30 – $50''$ and less broad at the higher offsets deeper into molecular clump. We note a narrow dark line at $V_{\text{lsr}} = -7.5 \text{ km s}^{-1}$, which we relate to self-absorption effect caused by the large-scale foreground material extended over RCW 120 and described in Sec. 1. Stratified structure of PDR and a transition from atomic to molecular gas can be seen from comparison of the CO(6–5) and archival [C II] pv diagrams, also shown in Fig. 8. We find the [C II] peak closer to the ionization front than the CO(6–5) peak at the pv diagram 1p. However, the [C II] and CO(6–5) peaks coincide at diagram 2p. We will discuss properties of the C⁺/CO transition of the PDR in Sec. 6.

Pv diagrams, made parallel to the ionization front, distinguish regions of the large-scale shocked layer and dense molecular clump. The diagrams 1 and 2 show a straight line at -8 km s^{-1} which makes a red-shifted arch up to -2 km s^{-1} at the offsets 60–110''. The arch becomes double-sided in diagrams 3 and 4 between the same offsets. The broadest CO(6–5) lines appear in positions of YSOs. Comparing the diagrams 3 and 4 with the line profiles in Fig. 4, we relate these broad lines to outflows to the red and blue sides, accompanying the star formation process towards the YSOs. Therefore, from these pv diagrams we distinguish two regions: the first one is regular structure related to the large-scale shocked layer from the expanding RCW 120 (at the offsets $< 60''$ and $> 110''$) and the second one related to star-forming regions in the dense clump.

Outflow candidates, detected by us in the present study, do not look like those that were found previously by Figueira et al. (2020) with low excitation CO(3–2) line. Therefore, we show the candidates in Fig. 9 considering the same velocity intervals as it was done for the CO(3–2) line. We find not one but several candidates using two times higher angular resolution. The first candidate, related with the S2 YSO, appears as an outflow oriented along the line of sight as the red and blue lobes almost coincide. Different geometry visible with the higher excitation lines can be related with the complex structure of the outflow near and far from the exciting source, traced by the (6–5) and (3–2) transitions, respectively. We find intersecting red and blue patches toward the S1 YSO where the blue-shifted part is much brighter than the red one. The red wings of methanol lines were seen previously by Kirsanova et al. (2021), therefore we do not have doubts about the outflow activity there. We deduced from emission maps of CH₃OH, SiO and DCO⁺ molecules (Plakitina et al., in prep.), that only red and blue patches around S1 and S2 are real outflows, but the other ones visible between S9, S10 and S39 are parts of complex kinematic structure of the region.

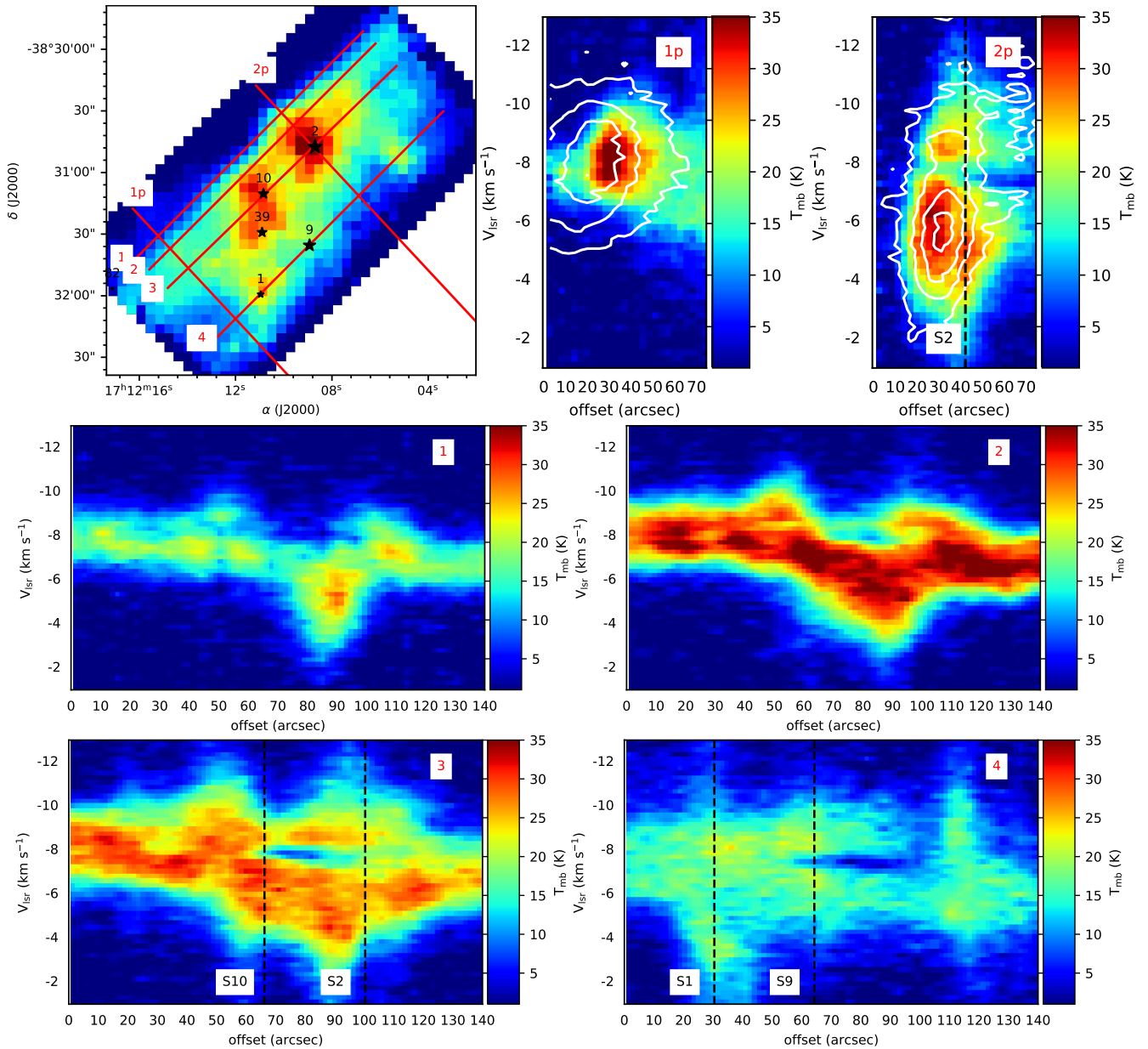


Figure 8. Pv diagrams of the CO(6–5) line emission. Top row: map of the integrated CO(6–5) emission where red lines show directions of the pv diagrams. Pv diagrams for the CO(6–5) (color) and [C II] lines (white contours), taken perpendicular to the ionization front are given on two right panels (1p and 2p). Middle and bottom rows: pv diagrams taken parallel to the ionization front (1–4). Black dashed lines show positions of YSOs on the pv diagrams, names of those are given in black.

6 DISCUSSION

We know that stellar wind (Luisi et al. 2021) and ionized gas (Sánchez-Cruces et al. 2018) expel all neutral material and produce dense expanding PDR around the bubble. The appearance of a dense layer, swiped by the shock wave, in the neutral side of PDR accompanies the expansion (Spitzer 1978, see also calculations by e.g. Hosokawa & Inutsuka (2005); Kirsanova et al. (2009); Akimkin et al. (2015); Bron et al. (2018)). We associate our bright CO-layer with the shocked molecular layer, moving away from the ionizing star, as we have shown above. While the bubble and the PDR resembles a sphere, the molecular region certainly has different geometry and resembles a flattened envelope oriented face-on which can be modelled in the plane-parallel approach.

Abundance of CO in the shocked layer agrees with the elemental value for this part of the Galaxy, it means that carbon is locked in this gas-phase CO. Since the position of the H₂ dissociation front normally coincides with the bright 8 μ m emission from PAHs (e. g. Fleming et al. 2010; Kaplan et al. 2021), we conclude that the CO and H₂ dissociation fronts are situated on the inner border of the bright CO(6–5) layer. The merged fronts appear as a natural consequence of the ongoing propagation of the dissociation fronts through the dense molecular cloud (see e. g. simulations by Störzer & Hollenbach 1998; Hosokawa & Inutsuka 2005; Kirsanova & Wiebe 2019): the denser the gas the closer the fronts. The pv diagrams from Fig. 8, taken perpendicular to the ionization front, confirm the merging of the H₂ and CO dissociation fronts in the dense material. For instance, comparing the diagram 1p and 2p, taken outside and through the

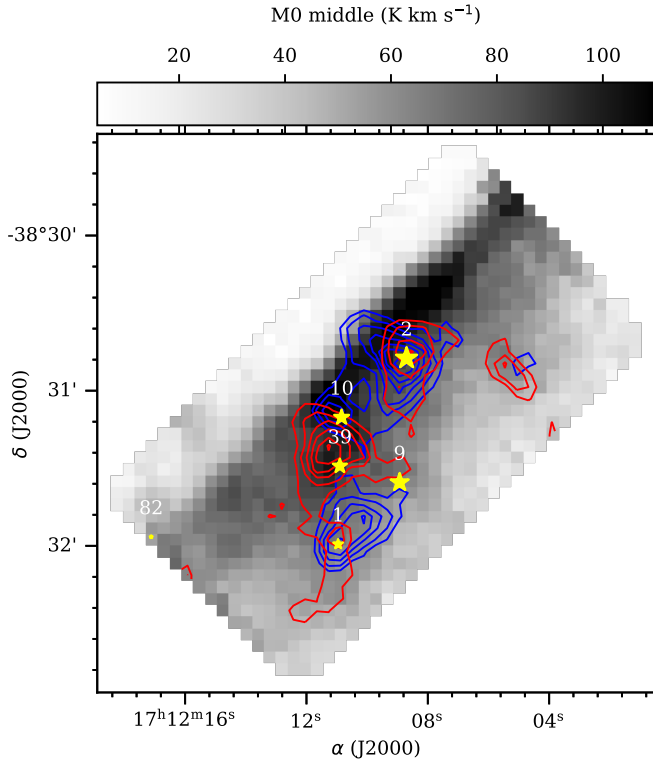


Figure 9. Channel maps of the CO(6–5) emission around RCW 120. There are three velocity intervals in this map: $V_{\text{lsr}} < -9$ (blue contours), $-9 < V_{\text{lsr}} < -4$ (middle, shown by greyscale) and $V_{\text{lsr}} > -4$ km s^{-1} (red contours). The contours are shown from 30 to 90 K km s^{-1} through 10 K km s^{-1} .

dense material, respectively, we find different separation between the [C II] and CO(6–5) peaks. The peaks do not coincide in the diagram 1p, but they merge in the diagram 2p. Taking into account divergence of the CO(6–5), [C II] and 8 μm peaks in the southeastern part of the observed region, we suggest that the CO and H₂ dissociation fronts might be separated there.

The shocked molecular gas appears as the most regular structure in our maps of the line emission in Fig. 2 and pv diagrams in Fig. 8. While the line width is still non-thermal, its value is about a factor of 2 lower in the shocked layer than in the molecular clump. Significant broadening of the molecular lines occurs near YSOs and is related to outflows. The shock does not disperse the dense clump unlike the outflows. This scenario looks similar to the recent findings by Kavak et al. (2022) in the Orion region and can be widespread around O-type stars surrounded by younger star-forming regions. Comparing the positions of YSOs found by Deharvang et al. (2009); Figueira et al. (2017) with the location of the dense shocked layer (see Fig. 3) we agree with conclusion by Figueira et al. (2020) that the YSOs were pre-existed before the shock wave from RCW 120 reached the molecular clump.

7 CONCLUSIONS

In this study, we made spatially and velocity-resolved observations of the RCW 120 PDR and nearby molecular gas with CO(6–5) and ¹³CO(6–5) lines and found a bright CO-emitting layer towards the PDR. We simulated physical conditions and emission of several CO and C+ lines in the RCW 120 PDR and found reasonable agreement

with the observed values. Based on this agreement, we related the CO-bright layer with shocked molecular gas moving away from the ionizing star due to expansion of H II region. While the shock itself is not visible, we found its impact on the neutral material around RCW 120 in our CO(6–5) map. We distinguished between large-scale structures and kinematical features such as the shocked gas and local ones such as dense environments of embedded protostars and outflows. We found the shocked layer as the most regular structure on the CO(6–5) map and in the velocity space, whereas the gas around YSOs was dispersed by the outflows.

ACKNOWLEDGEMENTS

We are thankful to S. V. Salii and K. V. Plakitina for fruitful discussions. We also thank unknown referee for his/her very relevant comments.

Based on observations with the Atacama Pathfinder EXperiment (APEX) telescope. APEX is a collaboration between the Max Planck Institute for Radio Astronomy, the European Southern Observatory, and the Onsala Space Observatory. Swedish observations on APEX are supported through Swedish Research Council grant No 2017-00648.

M. S. K. and Ya. N. P. were supported by RSCF, project number 21-12-00373. D. A. S. acknowledges financial support by the Deutsche Forschungsgemeinschaft through SPP 1833: "Building a Habitable Earth" (SE 1962/6-1). A. F. P. acknowledges the support of the Russian Ministry of Science and Education via the State Assignment Contract no. FEUZ-2020-0038.

DATA AVAILABILITY

Calibrated data on CO(6–5) and ¹³CO(6–5) emission generated in the study can be found in the ESO Archive (projects O-0103.F-9301A-2020 and O-0107.F-9318A-2021). Results of the calculations with MARION are available in Zenodo, at <https://zenodo.org/record/7447109>.

REFERENCES

- Akimkin V. V., Kirsanova M. S., Pavlyuchenkov Y. N., Wiebe D. S., 2015, *MNRAS*, **449**, 440
- Anderson L. D., et al., 2015, *ApJ*, **800**, 101
- Astropy Collaboration et al., 2013, *A&A*, **558**, A33
- Astropy Collaboration et al., 2018, *AJ*, **156**, 123
- Baryshev A. M., et al., 2015, *A&A*, **577**, A129
- Belitsky V., et al., 2018, *A&A*, **612**, A23
- Berné O., et al., 2022, *PASP*, **134**, 054301
- Bock D. C.-J., Large M. I., Sadler E. M., 1999, *AJ*, **117**, 1578
- Bron E., Agúndez M., Goicoechea J. R., Cernicharo J., 2018, arXiv e-prints, p. arXiv:1801.01547
- Deharvang L., Zavagno A., Schuller F., Caplan J., Pomarès M., De Breuck C., 2009, *A&A*, **496**, 177
- Drew J. E., et al., 2005, *MNRAS*, **362**, 753
- Figueira M., et al., 2017, *A&A*, **600**, A93
- Figueira M., Zavagno A., Bronfman L., Russeil D., Finger R., Schuller F., 2020, *A&A*, **639**, A93
- Fleming B., France K., Lupu R. E., McCandliss S. R., 2010, *ApJ*, **725**, 159
- Gaustad J. E., McCullough P. R., Rosing W., Van Buren D., 2001, *PASP*, **113**, 1326
- Goicoechea J. R., et al., 2016, *Nature*, **537**, 207
- Hosokawa T., Inutsuka S.-i., 2005, *ApJ*, **623**, 917
- Kabanovic S., et al., 2022, *A&A*, **659**, A36

- Kaplan K. F., Dinerstein H. L., Kim H., Jaffe D. T., 2021, *ApJ*, **919**, 27
- Kavak Ü., Goicoechea J. R., Pabst C. H. M., Bally J., van der Tak F. F. S., Tielens A. G. G. M., 2022, *A&A*, **660**, A109
- Kirsanova M. S., 2018, in Bisikalo D. V., Wiebe D. S., eds, *A.A. Boyarchuk Memorial Conference*. pp 284–289, doi:10.26087/INASAN.2018.1.1.048
- Kirsanova M. S., Wiebe D. S., 2019, *MNRAS*, **486**, 2525
- Kirsanova M. S., Wiebe D. S., Sobolev A. M., 2009, *Astronomy Reports*, **53**, 611
- Kirsanova M. S., Pavlyuchenkov Y. N., Wiebe D. S., Boley P. A., Salii S. V., Kalenskii S. V., Sobolev A. M., Anderson L. D., 2019, *MNRAS*, **488**, 5641
- Kirsanova M. S., Salii S. V., Kalenskii S. V., Wiebe D. S., Sobolev A. M., Boley P. A., 2021, *MNRAS*, **503**, 633
- Kuhn M. A., Hillenbrand L. A., Sills A., Feigelson E. D., Getman K. V., 2019, *ApJ*, **870**, 32
- Ladeyschikov D. A., Kirsanova M. S., Sobolev A. M., Thomasson M., Ossenkopf-Okada V., Juvela M., Khaibrakhmanov S. A., Popova E. A., 2021, *MNRAS*, **506**, 4447
- Luisi M., et al., 2021, *Science Advances*, **7**, eabe9511
- Mangum J. G., Shirley Y. L., 2015, *PASP*, **127**, 266
- Marsh K. A., et al., 2017, *MNRAS*, **471**, 2730
- Martins F., Pomarès M., Deharveng L., Zavagno A., Bouret J. C., 2010, *A&A*, **510**, A32
- McLeod A. F., Weibacher P. M., Ginsburg A., Dale J. E., Ramsay S., Testi L., 2016, *MNRAS*, **455**, 4057
- Molinari S., et al., 2010, *PASP*, **122**, 314
- Robitaille T., 2019, *APLpy v2.0: The Astronomical Plotting Library in Python*, doi:10.5281/zenodo.2567476, <https://doi.org/10.5281/zenodo.2567476>
- Robitaille T., Bressert E., 2012, *APLpy: Astronomical Plotting Library in Python*, *Astrophysics Source Code Library* (ascl:1208.017)
- Russeil D., 2003, *A&A*, **397**, 133
- Sánchez-Cruces M., Castellanos-Ramírez A., Rosado M., Rodríguez-González A., Reyes-Iturbide J., 2018, *Rev. Mex. Astron. Astrofis.*, **54**, 375
- Schneider N., et al., 2020, *PASP*, **132**, 104301
- Schuller F., et al., 2009, *A&A*, **504**, 415
- Spitzer L., 1978, *Physical processes in the interstellar medium*. Wiley-Interscience, New York, doi:10.1002/9783527617722
- Störzner H., Hollenbach D., 1998, *ApJ*, **495**, 853
- Tielens A. G. G. M., Hollenbach D., 1985, *ApJ*, **291**, 747
- Tielens A. G. G. M., Meixner M. M., van der Werf P. P., Bregman J., Tauber J. A., Stutzki J., Rank D., 1993, *Science*, **262**, 86
- Van der Tak F. F. S., Black J. H., Schöier F. L., Jansen D. J., van Dishoeck E. F., 2007, *A&A*, **468**, 627
- Walch S., Whitworth A. P., Bisbas T. G., Hubber D. A., Wünsch R., 2015, *MNRAS*, **452**, 2794
- Wall J. V., Jenkins C. R., 2003, *Practical Statistics for Astronomers*. Cambridge Observing Handbooks for Research Astronomers, Cambridge University Press, doi:10.1017/CBO9780511536618
- Wilson T. L., 1999, *Reports on Progress in Physics*, **62**, 143
- Zavagno A., Pomarès M., Deharveng L., Hosokawa T., Russeil D., Caplan J., 2007, *A&A*, **472**, 835

This paper has been typeset from a $\text{\TeX}/\text{\LaTeX}$ file prepared by the author.